High-Performance Midwave Type-II Superlattice Infrared Photodetectors With a Stepped InAs/GaSb Absorber

Qi Yuan, Chuang Li, Daqian Guo, Xinyue Cui, Xingyu Tang, Kai Shen, *Member, IEEE*, Jiang Wu, *Senior Member, IEEE*, and Zhiming Wang, *Senior Member, IEEE*

Abstract—Due to the short carrier diffusion length, the extraction of photogenerated carriers is one of the key issues in InAs/GaSb superlattice (SL) photodetectors. Here, we report a midinfrared InAs/GaSb SL absorber with a stepped band alignment. The stepped absorber facilitates a better carrier extraction efficiency. Simulation results show that the proposed nBn detector with a stepped absorber exhibited a substantial performance improvement over the nBn detectors with uniform absorbers. At 150 K, the detector with a 3.6-μm-thick stepped absorber has a maximum quantum efficiency (QE) of $\sim$46%, which is about 16% higher than that of the detectors with uniform absorbers. The maximum specific detectivity reached $\sim$4.26 $\times$ 10^{10} cm·Hz$^{1/2}$/W at 4.9 μm under -0.2 V bias. With the enhanced carrier extraction efficiency, the detectivity can gained a further improvement with a thicker stepped absorber, unlike the detector with a uniform absorber where the detectivity deteriorated with the absorber thickness increased from 3.6 to 4.2 μm.

Index Terms—InAs/GaSb, nBn photodetector, quantum efficiency (QE), type-II superlattices (T2SLs).

I. INTRODUCTION

TYPE-II superlattices (T2SLs) have attracted great attention for the development of high-performance infrared photodetectors, especially for midwave infrared (MWIR)

detection applications, including night vision, infrared imaging, and infrared guidance [1], [2], [3]. Motivated by the tunable bandgap, large carrier effective mass, low Auger recombination rate, and high material uniformity [4], [5], [6], T2SLs, and in particular InAs/GaSb superlattices (SLs), serve as an alternative to the well-established HgCdTe (MCT) and InSb for high operating temperature (HOT) MWIR infrared photodetectors [7], [8].

InAs/GaSb-based focal plane arrays have shown excellent performance in the MWIR spectral regions [1], [9], [10], [11]. However, the relatively high noise and restricted extraction capacity of photogenerated carriers from the active region greatly limit the further performance improvement of MWIR InAs/GaSb detectors. First, the diffusion current, generation–recombination (G–R) dark current associated with the Shockley–Read–Hall (SRH) recombination, trap-assisted tunneling current, and leakage current via surface states of the sidewalls are the main mechanisms of noise dark currents, which greatly degrade the overall device performance [12]. Since the barrier architecture was put forward [13], it has been extensively applied to InAsSb, MCT, and T2SLs photodetectors [3], [14], [15], [16], [17]. With the insertion of wide bandgap barrier layers, the surface leakage current can be effectively eliminated. In addition, the depletion region is almost confined in the wide bandgap barrier layers, by which the G–R dark current is significantly suppressed [10], [18]. As a result, benefiting from bandgap engineering, InAs/GaSb SLs barrier photodetectors exhibit significantly low dark current density compared to conventional devices with p-n or p-i-n architectures [3], [10]. Second, one major disadvantage of InAs/GaSb SLs is the short minority carrier lifetime compared with MCT and InSb [19], [20], resulting in a short carrier diffusion length [21]. A short carrier diffusion length certainly inhibits the extraction of photogenerated carriers from the active layers, making it a key issue for realizing high quantum efficiency (QE) of InAs/GaSb SLs photodetectors. Therefore, limited by the carrier transport, high detection performance cannot be achieved by increasing the thickness of the InAs/GaSb active layers. Consequently, to obtain a high-performance MWIR InAs/GaSb SLs detector, it is essential to suppress the dark current and enhance the transport of photogenerated carriers.

This article has been accepted for inclusion in a future issue of this journal. Content is final as presented, with the exception of pagination.

2   IEEE TRANSACTIONS ON ELECTRON DEVICES

TABLE I

PARAMETERS USED IN MODELING OF InAs/GaSb SLs DEVICES [22], [23], [24]

Parameter	Symbol (unit)	InAs	GaSb	$Al_xGa_{1-x}Sb$
Lattice constant	a (Å)	6.0522	6.0854	$6.0854+0.0443x$
Bandgap at 150 K	E_g (eV)	0.391	0.780	$0.78+0.886x$
Spin-orbit split-off energy	Δ (eV)	0.39	0.76	/
Electron effective mass	m_e/m_0	0.030	0.042	$0.042+0.188x$
Hole effective mass	m_h/m_0	0.414	0.412	$0.412+0.356x$
Luttinger parameters				
	γ_1	20.0	13.4	/
	γ_2	8.5	4.7	/
	γ_3	9.2	6.0	/
Optical matrix parameter	E_p (eV)	21.5	22.4	/
Valence band offset (w.r.t. GaSb)	VBO (eV)	-0.56	0	$-0.38x$
Deformation potentials				
	a_c (eV)	-5.08	-7.5	/
	a_v (eV)	-1	-0.8	/
	b (eV)	-1.8	-2	/
Elastic stiffness constant				
	C_{11} (10^{11} dyn/cm^2)	8.329	8.842	/
	C_{12} (10^{11} dyn/cm^2)	4.526	4.026	/

In this article, due to the tunability of electron and hole minibands by modifying the thickness of constituent layers, an nBn InAs/GaSb T2SLs MWIR photodetector with a stepped absorber is proposed to enhance the extraction of photogenerated carriers from the active layers. Due to the miniband offsets, an electric field is introduced in the stepped absorber, which promotes the carrier transport, improving the peak QE, responsivity, and specific detectivity (D^*). In addition, D^* can be further improved by increasing the thickness of the stepped absorber layers.

II. SIMULATION PROCEDURE

The simulations were performed by using APSYS software from Crosslight Inc. The zincblende 8×8 kp model was used to calculate the subband structures, in which an envelope function approximation formalism was employed [23]. The states throughout the Brillouin zone were evaluated. The optical properties of SLs were calculated based on the Fermi's golden rule. Following that, the Poisson equation and continuity equation were applied to monitor the complex light absorption and carrier dynamics in the detectors. The parameters of varied materials used in the simulation are listed in Table I. In addition, the lifetimes of both electron and hole are 50 ns [25], and the mobilities of electron and hole are 3000 and 600 cm^2·V^{-1}·s^{-1} [26], respectively.

The schematic of the nBn InAs/GaSb SLs photodetector with a stepped absorber ($S1$) is shown in Fig. 1. It consists of a 0.2-μm-thick 10-ML InAs/9-ML GaSb SLs n-type bottom contact layer on a GaSb substrate. Following is the 3.6-μm-thick stepped absorber, which is composed of a 1.1-μm-thick 10-ML InAs/9-ML GaSb SLs, a 1.1-μm-thick 10-ML InAs/10-ML GaSb SLs, and a 1.4-μm-thick 11-ML InAs/19-ML GaSb SLs. Finally, a 0.2-μm-thick $Al_{0.1}Ga_{0.9}Sb$ layer is chosen as the barrier, followed by a 0.15-μm-thick
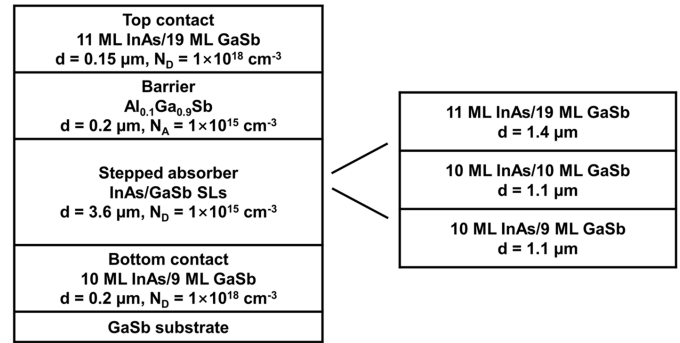

Fig. 1. Schematic of an nBn InAs/GaSb SLs device with a stepped absorber ($S1$).

11-ML InAs/19-ML GaSb SLs top contact. Three nBn detectors with different uniform absorbers (10-ML InAs/9-ML GaSb, 10-ML InAs/10-ML GaSb, and 11-ML InAs/19-ML GaSb SLs) are considered as references and the structures of detectors are listed in Table II.

For InAs/GaSb SLs, the electronic position of minibands can be tuned by changing the thickness of constituent layers. The effective miniband gaps of artificial SLs are determined by the lowest electron minibands and the highest hole minibands. As shown in Fig. 2, for 10-ML InAs/9-ML GaSb SLs, the miniband gap is $\sim$234 meV. Increasing the GaSb thickness from 9 to 10 ML would slightly widen the effective miniband gap to $\sim$235 meV. Since the holes are almost confined in the GaSb, the top of HH1 increases with the thickening of the GaSb layer. With increasing the GaSb to InAs ratio and period thickness, the effective miniband gap is reduced to $\sim$220 meV for 11-ML InAs/19-ML GaSb SLs. Meanwhile, the joint density of states for electrons and holes get more dispersed, and a reduction in the absorption coefficient and a red shift

This article has been accepted for inclusion in a future issue of this journal. Content is final as presented, with the exception of pagination.

YUAN et al.: HIGH-PERFORMANCE MIDWAVE T2SL INFRARED PHOTODETECTORS

3

TABLE II
STRUCTURES OF FOUR InAs/GaSb SLS DEVICES

|	Bottom contact d=0.2 μm N_D=1×10^{18} cm^{-3}	Absorber d=3.6 μm N_D=1×10^{15} cm^{-3}	Barrier d=0.2 μm N_A=1×10^{15} cm^{-3}	Top contact d=0.15 μm N_D=1×10^{18} cm^{-3}
S1	10 ML InAs/9 ML GaSb	Stepped absorber	Al$_{0.1}$Ga$_{0.9}$Sb	11 ML InAs/19 ML GaSb
U1	10 ML InAs/9 ML GaSb	10 ML InAs/9 ML GaSb	Al$_{0.1}$Ga$_{0.9}$Sb	10 ML InAs/9 ML GaSb
U2	10 ML InAs/10 ML GaSb	10 ML InAs/10 ML GaSb	Al$_{0.1}$Ga$_{0.9}$Sb	10 ML InAs/10 ML GaSb
U3	11 ML InAs/19 ML GaSb	11 ML InAs/19 ML GaSb	Al$_{0.1}$Ga$_{0.9}$Sb	11 ML InAs/19 ML GaSb
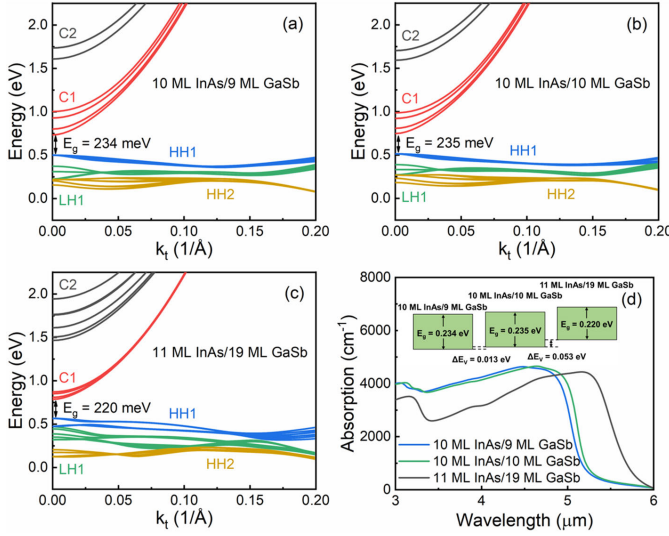
Fig. 2. Energy dispersion diagrams of (a) 10-ML InAs/9-ML GaSb, (b) 10-ML InAs/10-ML GaSb, and (c) 11-ML InAs/19-ML GaSb SLs at 150 K, and the zero energy reference is chosen as the valence band edge of InAs. (d) Absorption coefficients of three InAs/GaSb SLs at 150 K. Inset: Schematic band alignment of three InAs/GaSb SLs.
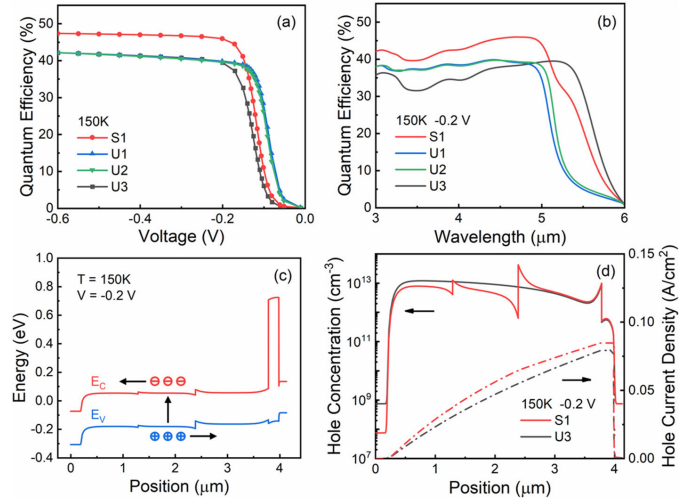

Fig. 3. (a) QE versus voltage of four devices. (b) QE versus wavelength of four devices. (c) Energy band diagram under bias of $S1$. (d) Hole concentration and hole current density of $S1$ and $U3$.

of the light absorption spectrum are expected [27], [28]. Due to the weak overlap of electron wave functions, a decrease in the conduction bandwidth ($\Delta C1$) as well as an increase in the bottom of $C1$ is obtained in thick SL periods [29]. Consequently, due to the discontinuity of the conduction and valence minibands of the three InAs/GaSb SLs, an electric field can be introduced by applying a stepped absorber [30].

In device $S1$, the three adopted InAs/GaSb SLs share similar miniband gaps of ∼0.230 eV (∼5.5 μm) at 150 K. The absorption coefficients of the three InAs/GaSb SLs are ∼4600 cm^{-1} in the MWIR regions, which are consistent with previous experimental results [28], [31], [32].

III. DEVICE PERFORMANCE AND ANALYSIS

The voltage-dependent QE (QE versus V) and wavelength-dependent QE (QE versus λ) results are plotted in Fig. 3(a) and (b), respectively. The quantum efficiencies of devices increase with the reverse bias voltage and get saturated at about −0.2 V. Device $S1$ shows the highest QE in the wavelength region from 3.0 to 5.0 μm under −0.2 V reverse bias at 150 K indicating an enhanced carrier extraction efficiency with the stepped absorber. The maximum QE of $S1$ reaches ∼46% at 4.7 μm, which is ∼16% higher than all the three reference devices with a

uniform absorber. Within the wavelength range from 3.0 to 5.0 μm, the light absorption coefficient of 11-ML InAs/19-ML GaSb SLs is lower than that of 10-ML InAs/9-ML GaSb SLs and 10-ML InAs/10-ML GaSb SLs, resulting in a lowest QE in device $U3$. Due to different cutoff wavelengths of varied InAs/GaSb SLs profiles [as shown in Fig. 2(d)], a red shift in the QE spectra of $U3$ is observed, and the maximum QE of ∼39% is obtained at 5.2 μm. For $S1$, due to the different bandgaps and light absorption coefficients of the three adopted InAs/GaSb SLs, the cutoff edge in the long wavelength region is not as steep as the other three devices. Because of lower valence band offsets at absorber/barrier interfaces, the QEs of $U1$ and $U2$ could get saturated under a smaller reverse bias. Considering the response spectrum, $U3$ is chosen as the main reference device in the subsequent discussion.

The energy band alignment, the hole concentration, and hole current density distribution in the devices under −0.2 V bias and illumination are illustrated in Fig. 3(c) and (d). Due to the valence band and conduction band offsets between the three InAs/GaSb SLs, an electric field is generated, resulting in lower hole density in device $S1$. The electric field in the stepped absorber of $S1$ can effectively promote the transport of photogenerated carriers. Therefore, device $S1$ exhibits higher photocurrent and improved QE, which is consistent with our results.

The temperature-dependent dark current density (J_d) versus voltage curves are illustrated in Fig. 4(a). The J_d of both
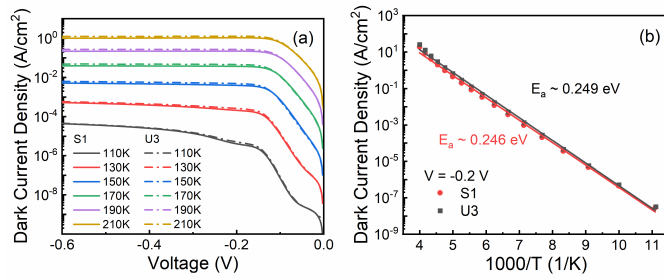
This article has been accepted for inclusion in a future issue of this journal. Content is final as presented, with the exception of pagination.

4   IEEE TRANSACTIONS ON ELECTRON DEVICES

Fig. 4.   (a) Dark current density as a function of applied bias voltage for $S1$ and $U3$ with temperatures ranging from 110 to 210 K and (b) Arrhenius plots of the dark current density under -0.2 V bias. Solid lines represent the linear fit at different temperatures.
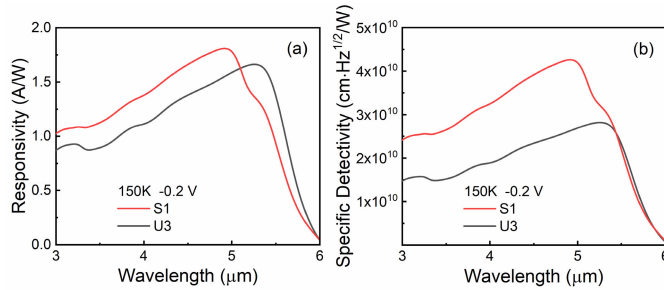

Fig. 5.   (a) Responsivity and (b) specific detectivity of $S1$ and $U3$ at 150 K and under -0.2 V bias voltage.

Fig. 6.   Specific detectivity of $S1$ and $U3$ with varied absorber thicknesses for $T = 150$ K and $V = -0.2$ V.

devices rises sharply with the increasing temperature due to the increased intrinsic carrier density, and the J_d of $S1$ is slightly lower than $U3$. At 150 K and under -0.2 V bias voltage, the J_d values of $S1$ and $U3$ are $\sim 3.9 \times 10^{-3}$ and $\sim 4.8 \times 10^{-3}$ A/cm^2, respectively. When the reverse bias voltage exceeds -0.2 V, the J_d values reach a plateau of $\sim 5.1 \times 10^{-3}$ A/cm^2 for $S1$ and $\sim 6.2 \times 10^{-3}$ A/cm^2 for $U3$. The hole density in $S1$ is lower than that in $U3$, which may be responsible for the lower dark current in $S1$. Fig. 4(b) shows the temperature-dependent Arrhenius plots of J_d under -0.2 V bias. The estimated activation energies (E_a) of $S1$ and $U3$ are ~ 0.246 and ~ 0.249 eV, respectively, which are close to the effective bandgap ~ 0.250 eV of three adopted InAs/GaSb SLs at 77 K [33]. It indicates that the dark currents of both devices are dominated by the carrier diffusion mechanism [34].

The 50% cutoff wavelengths of $S1$ and $U3$ are 5.5 and 5.7 μm, respectively, as illustrated in Fig. 5(a). At 150 K and under -0.2 V bias voltage, the maximum R is ~ 1.81 A/W at 4.9 μm for $S1$, which is $\sim 9\%$ higher than the $U3$ where the maximum R is ~ 1.66 A/W at 5.3 μm. Accordingly, as shown in Fig. 5(b), the maximum specific detectivity (D^*) of $S1$ reaches $\sim 4.26 \times 10^{10}$ cm·Hz$^{1/2}$/W at 4.9 μm, which is $\sim 53\%$ higher than that of $\sim 2.79 \times 10^{10}$ cm·Hz$^{1/2}$/W at 5.3 μm for $U3$ at 150 K and -0.2 V bias voltage. With similar 50% cutoff wavelengths, $S1$ exhibits higher D^* in nearly the entire MWIR region.

The dark current density has an almost linear relationship with the thickness of absorber layer, which in return is directly associated with the light absorption in the device [7]. Therefore, a tradeoff between photogenerated carriers and dark current density is essential in high-performance detectors. $U3$ exhibits optimal performance with a uniform absorber
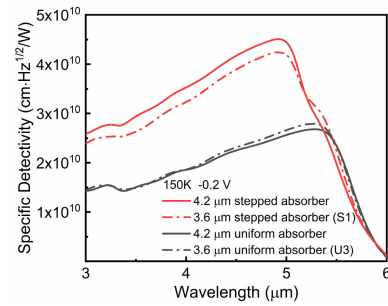
layer thickness of 3.6 μm. Increasing the thickness of uniform absorber from 3.6 to 4.2 μm would not bring about an improvement in QE due to the limited carrier diffusion length of InAs/GaSb SLs [21]. On the contrary, a reduction in D^* of the device with a 4.2-μm uniform absorber is observed as the J_d rises, as illustrated in Fig. 6. In $S1$, increasing the total thickness of the stepped absorber from 3.6 to 4.2 μm, which consists of a 1.5-μm-thick 10-ML InAs/11-ML GaSb, a 1.5-μm-thick 10-ML InAs/10-ML GaSb, and a 1.2-μm-thick 11-ML InAs/19-ML GaSb SLs, the maximum D^* can be further increased to $\sim 4.51 \times 10^{10}$ cm·Hz$^{1/2}$/W at 4.9 μm. Benefiting from the improved carrier transport in $S1$ by applying a stepped absorber, it provides a feasible method to further improve the performance of InAs/GaSb SLs infrared detectors.

IV. Conclusion

In summary, we have provided an insight of the InAs/GaSb SLs stepped absorber. The stepped absorber is proposed to enhance the carrier extraction from the absorber layers. The energy band alignments and optical properties of InAs/GaSb SLs with various periods are studied. As a result of the improvement of hole transport, the device with a stepped absorber exhibits a higher maximum QE of $\sim 46\%$ at 4.7 μm under -0.2 V bias at 150 K. The maximum D^* of the device with a stepped absorber is improved to $\sim 4.26 \times 10^{10}$ cm·Hz$^{1/2}$/W at 4.9 μm, which is $\sim 53\%$ higher than the device with a uniform absorber. Furthermore, benefiting from the more efficient carrier extraction, increasing the total thickness of the stepped absorber from 3.6 to 4.2 μm, the maximum D^* of detector can be further increased to $\sim 4.51 \times 10^{10}$ cm·Hz$^{1/2}$/W. A feasible method is proposed to further improve the performance of InAs/GaSb SLs infrared detectors.

References

[1] S. A. Pour, E. K. Huang, G. Chen, A. Haddadi, B.-M. Nguyen, and M. Razeghi, "High operating temperature midwave infrared photodiodes and focal plane arrays based on type-II InAs/GaSb superlattices," *Appl. Phys. Lett.*, vol. 98, no. 14, Apr. 2011, Art. no. 143501, doi: 10.1063/1.3573867.

[2] Y. Wei et al., "Uncooled operation of type-II InAs/GaSb superlattice photodiodes in the midwavelength infrared range," *Appl. Phys. Lett.*, vol. 86, no. 23, Jun. 2005, Art. no. 233106, doi: 10.1063/1.1947908.

[3] J. B. Rodriguez et al., "NBn structure based on InAs/GaSb type-II strained layer superlattices," *Appl. Phys. Lett.*, vol. 91, no. 4, Jul. 2007, Art. no. 043514, doi: 10.1063/1.2760153.

This article has been accepted for inclusion in a future issue of this journal. Content is final as presented, with the exception of pagination.

YUAN et al.: HIGH-PERFORMANCE MIDWAVE T2SL INFRARED PHOTODETECTORS 5

[4] D. Z. Ting, A. Soibel, and S. D. Gunapala, "Type-II superlattice hole effective masses," *Infr. Phys. Technol.*, vol. 84, pp. 102–106, Aug. 2017, doi: 10.1016/j.infrared.2016.10.014.

[5] H. Mohseni, V. I. Litvinov, and M. Razeghi, "Interface-induced suppression of the Auger recombination in type-II InAs/GaSb superlattices," *Phys. Rev. B, Condens. Matter*, vol. 58, no. 23, pp. 15378–15380, Dec. 1998, doi: 10.1103/PhysRevB.58.15378.

[6] D. Z. Ting et al., "Advances in III–V semiconductor infrared absorbers and detectors," *Infr. Phys. Technol.*, vol. 97, pp. 210–216, Mar. 2019, doi: 10.1016/j.infrared.2018.12.034.

[7] A. Rogalski, P. Martyniuk, and M. Kopytko, "Type-II superlattice photodetectors versus HgCdTe photodiodes," *Prog. Quantum Electron.*, vol. 68, Nov. 2019, Art. no. 100228, doi: 10.1016/j.pquantelec.2019.100228.

[8] A. Rogalski, "Recent progress in infrared detector technologies," *Infr. Phys. Technol.*, vol. 54, pp. 136–154, May 2011, doi: 10.1016/j.infrared.2010.12.003.

[9] H. S. Kim et al., "Mid-IR focal plane array based on type-II InAs/GaSb strain layer superlattice detector with nBn design," *Appl. Phys. Lett.*, vol. 92, no. 18, May 2008, Art. no. 183502, doi: 10.1063/1.2920764.

[10] E. Plis et al., "Mid-infrared InAs/GaSb strained layer superlattice detectors with nBn design grown on a GaAs substrate," *Semicond. Sci. Technol.*, vol. 25, no. 8, pp. 085010-1–085010-4, 2010, doi: 10.1088/0268-1242/25/8/085010.

[11] C. J. Hill, A. Soibel, S. A. Keo, J. M. Mumolo, D. Z. Ting, and S. D. Gunapala, "Demonstration of large format mid-wavelength infrared focal plane arrays based on superlattice and BIRD detector structures," *Infr. Phys. Technol.*, vol. 52, no. 6, pp. 348–352, Nov. 2009, doi: 10.1016/j.infrared.2009.09.007.

[12] E. Plis et al., "InAs/GaSb strained layer superlattice detectors with nBn design," *Infr. Phys. Technol.*, vol. 52, no. 6, pp. 335–339, Nov. 2009, doi: 10.1016/j.infrared.2009.09.008.

[13] S. Maimon and G. W. Wicks, "nBn detector, an infrared detector with reduced dark current and higher operating temperature," *Appl. Phys. Lett.*, vol. 89, no. 15, pp. 151109-1–151109-3, Oct. 2006, doi: 10.1063/1.2360235.

[14] A. Rogalski and P. Martyniuk, "Mid-wavelength infrared nBn for HOT detectors," *J. Electron. Mater.*, vol. 43, no. 8, pp. 2963–2969, Aug. 2014, doi: 10.1007/s11664-014-3161-y.

[15] E. Weiss et al., "InAsSb-based XB$_n$n *bariodes* grown by molecular beam epitaxy on GaAs," *J. Cryst. Growth*, vol. 339, no. 1, pp. 31–35, Jan. 2012, doi: 10.1016/j.jcrysgro.2011.11.076.

[16] A. M. Itsuno, J. D. Phillips, and S. Velicu, "Design and modeling of HgCdTe nBn detectors," *J. Electron. Mater.*, vol. 40, no. 8, pp. 1624–1629, 2011.

[17] Z. Deng, D. Guo, J. Huang, H. Liu, J. Wu, and B. Chen, "Mid-wave infrared InAs/GaSb type-II superlattice photodetector with n-B-p design grown on GaAs substrate," *IEEE J. Quantum Electron.*, vol. 55, no. 4, pp. 1–5, Aug. 2019, doi: 10.1109/JQE.2019.2917946.

[18] P. C. Klipstein, "Perspective on III–V barrier detectors," *Appl. Phys. Lett.*, vol. 120, no. 6, Feb. 2022, Art. no. 060502, doi: 10.1063/5.0084100.

[19] D. Donetsky, G. Belenky, S. Svensson, and S. Suchalkin, "Minority carrier lifetime in type-2 InAs–GaSb strained-layer superlattices and bulk HgCdTe materials," *Appl. Phys. Lett.*, vol. 97, no. 5, Aug. 2010, Art. no. 052108, doi: 10.1063/1.3476352.

[20] D. Donetsky, S. P. Svensson, L. E. Vorobjev, and G. Belenky, "Carrier lifetime measurements in short-period InAs/GaSb strained-layer superlattice structures," *Appl. Phys. Lett.*, vol. 95, no. 21, pp. 14–17, 2009, doi: 10.1063/1.3267103.

[21] P. C. Klipstein et al., "Minority carrier lifetime and diffusion length in type II superlattice barrier devices," *Infr. Phys. Technol.*, vol. 96, pp. 155–162, Jan. 2019, doi: 10.1016/j.infrared.2018.11.022.

[22] I. R. Vurgaftman, R. J. Meyer, and L. R. Ram-Mohan, "Band parameters for III–V compound semiconductors and their alloys," *J. Appl. Phys.*, vol. 89, no. 11, pp. 5815–5875, 2001, doi: 10.1063/1.1368156.

[23] P.-F. Qiao, S. Mou, and S. L. Chuang, "Electronic band structures and optical properties of type-II superlattice photodetectors with interfacial effect," *Opt. Exp.*, vol. 20, no. 3, pp. 2319–2334, Jan. 2012, doi: 10.1364/OE.20.002319.

[24] P. Martyniuk et al., "nBn T2SLs InAs/GaSb/B-AlGaSb HOT detector for fast frequency response operation," in *Proc. Conf. Optoelectron. Microelectron/ Mater. Devices*, Dec. 2014, pp. 226–229, doi: 10.1109/COMMAD.2014.7038697.

[25] B. Klein et al., "Carrier lifetime studies in midwave infrared type-II InAs/GaSb strained layer superlattice," *J. Vac. Sci. Technol. B, Microelectron. Process. Phenom.*, vol. 32, pp. 02C101-1–02C101-7, Jan. 2014, doi: 10.1116/1.4862085.

[26] F. Szmulowicz, H. J. Haugan, S. Elhamri, and G. J. Brown, "Calculation of vertical and horizontal mobilities in InAs/GaSb superlattices," *Phys. Rev. B, Condens. Matter*, vol. 84, no. 15, Oct. 2011, Art. no. 155307, doi: 10.1103/PhysRevB.84.155307.

[27] I. Vurgaftman et al., "Interband absorption strength in long-wave infrared type-II superlattices with small and large superlattice periods compared to bulk materials," *Appl. Phys. Lett.*, vol. 108, no. 22, May 2016, Art. no. 222101, doi: 10.1063/1.4953035.

[28] Y. Livneh et al., "k · p model for the energy dispersions and absorption spectra of InAs/GaSb type-II superlattices," *Phys. Rev. B, Condens. Matter*, vol. 86, no. 23, Dec. 2012, Art. no. 235311, doi: 10.1103/PhysRevB.86.235311.

[29] H. J. Haugan, F. Szmulowicz, G. J. Brown, and K. Mahalingam, "Band gap tuning of InAs/GaSb type-II superlattices for mid-infrared detection," *J. Appl. Phys.*, vol. 96, no. 5, pp. 2580–2585, Sep. 2004, doi: 10.1063/1.1776321.

[30] D. Z. Ting et al., "Long and very long wavelength InAs/InAsSb superlattice complementary barrier infrared detectors," *J. Electron. Mater.*, vol. 51, no. 9, pp. 4666–4674, Sep. 2022, doi: 10.1007/s11664-022-09561-3.

[31] J. B. Rodriguez, P. Christol, L. Cerutti, F. Chevrier, and A. Joullié, "MBE growth and characterization of type-II InAs/GaSb superlattices for mid-infrared detection," *J. Cryst. Growth*, vol. 274, nos. 1–2, pp. 6–13, Jan. 2005, doi: 10.1016/j.jcrysgro.2004.09.088.

[32] B. Klein et al., "Varshni parameters for InAs/GaSb strained layer superlattice infrared photodetectors," *J. Phys. D, Appl. Phys.*, vol. 44, no. 7, pp. 075102-1–075102-5, 2011, doi: 10.1088/0022-3727/44/7/075102.

[33] M. Delmas, B. Liang, and D. L. Huffaker, "A comprehensive set of simulation tools to model and design high-performance type-II InAs/GaSb superlattice infrared detectors," *Proc. SPIE*, vol. 10926, pp. 29–39, Feb. 2019, doi: 10.1117/12.2509480.

[34] P. Martyniuk, M. Kopytko, and A. Rogalski, "Barrier infrared detectors," *Opto-Electron. Rev.*, vol. 22, no. 2, pp. 127–146, 2014, doi: 10.2478/s11772-014-0187-x.